Journal of Groundwater Science and Engineering
ISSN 2305-7068
Indexed by ESCI CABI CSA
Scopus GeoRef AJ CNKI

Karst distribution characteristics in a watershed under topographic differentiation and implication for groundwater resource: A case study in Southwest China using ERT and borehole data

Zhan-yu Tang, De-qiu Dai, Wei-wei Jiang, Ren-jian Deng

Citation:
Tang ZY, Dai DQ, Jiang WW, Deng RJ. 2026. Karst distribution characteristics in a watershed under topographic differentiation and implication for groundwater resource: A case study in Southwest China using ERT and borehole data. Journal of Groundwater Science and Engineering, 14(3): 271-287.

View online: https://doi.org/10.26599/JGSE.2026.9280083

Articles you may be interested in

Investigation of groundwater characteristics and its influence on Landslides in Heifangtai Plateau using comprehensive geophysical methods
Journal of Groundwater Science and Engineering. 2023, 11(2): 171-182 https://doi.org/10.26599/JGSE.2023.9280015

Application of hydrochemistry and strontium isotope for understanding the hydrochemical characteristics and genesis of strontium-rich groundwater in karst area, Gongcheng County, Southwest China
Journal of Groundwater Science and Engineering. 2024, 12(3): 264-280 https://doi.org/10.26599/JGSE.2024.9280020

Effects of coal mining and tunnel excavation on groundwater flow system in karst areas by modeling: A case study in Zhongliang Mountain, Chongqing, Southwest China
Journal of Groundwater Science and Engineering. 2023, 11(4): 391-407 https://doi.org/10.26599/JGSE.2023.9280031

Evaluation of groundwater resource potential by using water balance model: A case of Upper Gilgel Gibe Watershed, Ethiopia
Journal of Groundwater Science and Engineering. 2022, 10(3): 209-222 https://doi.org/10.19637/j.cnki.2305-7068.2022.03.001

Modelling the monthly hydrological balance using Soil and Water Assessment Tool (SWAT) model: A case study of the Wadi Mina upstream watershed
Journal of Groundwater Science and Engineering. 2024, 12(2): 161-177 https://doi.org/10.26599/JGSE.2024.9280013

Determination of groundwater potential distribution in Kulfo-Hare watershed through integration of GIS, remote sensing, and AHP in Southern Ethiopia
Journal of Groundwater Science and Engineering. 2023, 11(3): 249-262 https://doi.org/10.26599/JGSE.2023.9280021

Journal homepage: http://gwse.iheg.org.cn

Research Article

Karst distribution characteristics in a watershed under topographic differentiation and implication for groundwater resource: A case study in Southwest China using ERT and borehole data

Zhan-yu Tang[1,2,3], De-qiu Dai[2*], Wei-wei Jiang[3], Ren-jian Deng[1]

[1] *School of Civil Engineering*, *Hunan University of Science and Technology*, *Xiangtan* 411201, *Hunan Province*, *China*.
[2] *School of Earth Sciences and Spatial Information Engineering*, *Hunan University of Science and Technology*, *Xiangtan* 411201, *Hunan Province*, *China*.
[3] *State Key Laboratory of Environmental Geochemistry*, *Institute of Geochemistry*, *Chinese Academy of Sciences*, *Guiyang* 550081, *China*.

Abstract: Karst landforms are renowned for their unique characteristics, and investigating karst development characteristics is of great significance for groundwater regulation and ecological management. This study aims to interpret karst distribution under different topographic conditions in a watershed using Electrical Resistivity Tomography (ERT). Taking the Chenqi small watershed in Southwest China as the study area, 10 ERT survey lines were deployed across three topographic settings (dip slopes, anti-dip slopes, and high-lying depressions). By combining 2D/3D ERT inversion, geological drilling, and outcrop verification, the subsurface karst distribution was revealed. The results show that ERT effectively detects karst features with high heterogeneity and discontinuity. Conduit-type karst appears in the middle section of both slopes, indicating groundwater migration pathways. Karst water is dominated by runoff on dip slopes, whereas infiltration dominates on anti-dip slopes; continuous low-resistivity aquicludes in high-lying depressions control local groundwater levels. The average karst zone thickness is 2.0–4.0 m, with a maximum of 12 m. These findings demonstrate a coupled relationship between karst structure and groundwater runoff under topographic differentiation, providing a quantitative reference for watershed-scale groundwater processes and practical value for karst water exploration, resource regulation, and slope stability assessment.

Keywords: Hydrogeophysics; Electrical Resistivity Tomography (ERT); Geological drilling; Karst distribution characteristics; Groundwater processes

Received: 15 Dec 2025/ Accepted: 10 May 2026/ Published: 30 Jul 2026

Introduction

The groundwater ecological environment in Southwest China is relatively fragile, primarily attributed to karstification (An et al., 2026; Li et al., 2022). Karstification refers to the dissolution or deposition processes of carbonate rocks within the groundwater circulation system, while karst features are the imprints of this complex circulation system on carbonate rocks (Cao et al., 2018; Guo et al., 2024). Karst regions are widely distributed across China, where geological and environmental problems such as karst ground collapse, groundwater contamination, and ecological degradation frequently occur (Guo et al., 2013; Wang, 2024a; Yue et al., 2026; Zhao and Hou, 2019). Therefore, karst research is of great importance for understanding the formation mechanisms of karst landscapes, predicting karst hazards, and guiding the rational exploitation and utilization of groundwater resources (Lan et al., 2024; Wang et al., 2024b; Xiao et al., 2023). Traditional karst investigation methods primarily rely on field geological reconnaissance, outcrop lithological

*Corresponding author: De-qiu Dai, *E-mail address*: ddqygf@163.com

DOI: 10.26599/JGSE.2026.9280083

Tang ZY, Dai DQ, Jiang WW, et al. 2026. Karst distribution characteristics in a watershed under topographic differentiation and implication for groundwater resource: A case study in Southwest China using ERT and borehole data. Journal of Groundwater Science and Engineering, 14(3): 271-287.

2305-7068/© 2026 Journal of Groundwater Science and Engineering Editorial Office This is an open access article under the CC BY-NC-ND license (http://creativecommons.org/licenses/by-nc-nd/4.0)

analysis, and geological mapping, which infer subsurface conditions from surface observations alone. However, due to concealed and complex nature of karst strata, it is difficult to accurately characterize karst distribution characteristics (Li et al., 2023; Liu et al., 2024). In contrast, geophysical methods and geological drilling offer significant advantages. They provide higher resolution, greater subsurface detection capabilities, and more reliable identification of karst features. Geophysical techniques can accurately capture small-scale karst features and enable subsurface visualization, while drilling can provide direct physical evidence to complement the understanding of vertical karst distribution patterns. Therefore, employing diverse methodologies to delineate karst distribution patterns in karst regions holds significant scientific value and application prospects.

Geological drilling is an important method for detecting subsurface karst structures, and the core samples obtained from drilling are key data for studying karst development characteristics (Tan et al., 2024). However, geological drilling is difficult to deploy on steep slopes, making geophysical exploration based on physical property data the primary method for detecting karst features on karst slopes. Peng Tao et al., (2022) interpreted the spatial distribution of the epikarst zone in karst slopes using Ground Penetrating Radar (GPR) and explored potential indicators in radar data for identifying karst development depth through attribute analysis approaches (Gao et al., 2020). By analyzing GPR wave characteristics combined with complementary data, the location and geometric morphology of different karst types can be determined (Bermejo et al., 2020; Zhang et al., 2013). Nevertheless, GPR signals are highly susceptible to external interference, and its deployment conditions are relatively demanding. Therefore, several researchers, including Cheng Qinbo, Chen Xi, Min Tao, have adopted Electrical Resistivity Tomography (ERT) to quantify karst development and hydrological characteristics, and conducted a series of studies on the structure of the karst critical zone (Chen et al., 2018; Cheng et al., 2019a; Cheng et al., 2019b; Tao et al., 2022). ERT is easy to deploy and provides intuitive detection results, and has gradually become an important tool for characterizing karst features (Jiang et al., 2025). Luo et al. (2024) employed ERT to investigate soil distribution on karst slopes in Southwest China, observing the heterogeneous features of soil and the epikarst zone within the study area. Bouzerda et al. (2026) combined ERT with geomorphological analysis for karst hazard assessment, providing a powerful tool for risk mitigation and regional planning in collapse-prone karst environments. Additionally, ERT can be applied to determine bedrock depth and detect karst ground subsidence, serving as an important technique for underground structure exploration (Coulouma et al., 2013; Xie et al., 2022).

Although previous studies have made significant progress in applying ERT in karst regions, most have focused on a single lithology or a single slope (Bouzerda et al., 2026; Wanaim et al., 2025). At the scale of an entire watershed, systematic geophysical evidence is still lacking regarding karst features characterized by diverse topographic conditions and complex lithologies (Funk et al., 2024; Zhang et al., 2024). Therefore, this study selects the Chenqi small watershed in Southwest China, a site with distinctive characteristics, as a case study. First, within a small area, it encompasses a complete karst groundwater watershed system, allowing for more comprehensive detection of subsurface hydrological processes. Second, it simultaneously develops three topographic configurations (dip slopes, anti-dip slopes, and high-lying depressions), making topography a key variable, a feature rarely addressed simultaneously in existing karst studies. Third, it includes nearly all rock types found in karst regions. Although the lithology is complex, the stratigraphic boundaries are clearly delineated, enabling analysis of karst response mechanisms under complex geological conditions. Finally, as a typical rainfall driven karst watershed, it exhibits sensitive hydrological responses and is equipped with comprehensive hydrological monitoring infrastructure (Cheng et al., 2020; Zhang et al., 2019). These characteristics make the Chenqi Small Watershed an ideal site for studying the quantitative relationship between karst features and the groundwater system under complex geology and topographic differentiation. Such advantages are rarely seen in existing karst studies, and this constitutes the core innovation of this research.

The objectives of this study are to (1) quantify the depth, scale, and spatial distribution of karst development under different topographic conditions; (2) identify the resistivity response characteristics of karst features under different combinations of topography and lithology as revealed by ERT inversion; (3) reveal the implications of spatial karst distribution characteristics for groundwater resources at the watershed scale. To achieve these objectives, this study employs ERT as the primary method, with geological drilling and typical outcrops as validation tools. For the first time

in a karst region at the watershed scale, this study systematically analyzes karst distribution characteristics across an entire watershed based on three topographic types (dip slopes, anti-dip slopes, and high-lying depressions) and complex lithological structures, ultimately establishing a coupled relationship between karst structure and groundwater runoff under topographic differentiation. In addition, this study discusses the characteristics of karst differentiation in small watersheds, the applicability and limitations of ERT in karst research, and the influence of karst on groundwater resources. The research findings can provide high-resolution karst structure data for groundwater ecological environment assessment at the small watershed scale and offer a transferable research framework for karst regions exhibiting similar topographic differentiation characteristics.

1 Study area and methods

1.1 Study area

The study area is the Chenqi Small Watershed, located in the eastern part of Chenqibao Village, Puding County, Anshun City, Guizhou Province, China (26°15′36″–26°15′56″N, 105°43′30″–105°44′42″E). It is a typical karst underground river basin in Southwest China, as well as the first small watershed established for karst critical zone research and national field monitoring in the country. Covering an area of approximately 1.5 km^2, the watershed has a subtropical monsoon humid climate, with a multi-year average precipitation of 1,336 mm and a mean annual temperature of 14.2°C, featuring synchronous rainfall and heat. Surface water and groundwater increase markedly during the rainy season and converge from east to west at the watershed outlet. With an altitude ranging from 1,338 m to 1,491 m, the watershed exhibits a peak cluster depression landform enclosed by mountains on three sides, where karstification is extensively developed.

The strata in the study area are dominated by thick-bedded limestone, thin-bedded limestone intercalated with marl, and a small amount of dolomitic limestone from the 2nd and 3rd submembers of the 2nd member of the Middle Triassic Guanling Formation (Chen et al., 2018). The rock layers dip toward the northwest-northwest (approximately 280°) with a gentle inclination angle (about 7°), belonging to soluble rocks. The dominant soil types are limestone soil and clay. The limestone exhibits a thin-to-thick double bedding structure, and the intercalations and interbeddings have led to extensive fracture development. Coupled with the subtropical monsoon humid climate, characterized by abundant precipitation and warm, humid conditions during the rainy season, these factors provide favorable conditions for karstification and groundwater migration.

Groundwater, karst water, and spring water in the Chenqi Small Watershed all originate from atmospheric precipitation. Analysis of the remote sensing topographic map (Fig. 1) shows that the watershed is enclosed by mountains on three sides, with only the western side being flat and serving as the outlet. All slopes serve as primary channels for karst water migration and surface water runoff. Gaozita, a special distinctive depression, is located at a relatively high elevation in the upper slope position of the entire watershed. A large-scale aquifuge exists in this area and has been preserved through prolonged geological tectonic processes. Blocked by the aquiclude, part of the water is trapped and converges into the Chenqi Small Watershed via surface ditches and karst infiltration. To investigate the karst distribution characteristics of the karst small watershed, three sites were selected: Yang slope (anti-dip slope, northeastern part of the watershed), Huoshao slope (dip slope, southeastern part of the watershed), and Gaozita (high-lying depression, southern part of the watershed). These sites cover the three main karst development areas and karst fissure water enrichment zones within the watershed. Fig. 1 presents relevant information for the Chenqi watershed. The geographical location map is adapted from China Map GS (2019) No. 1617, and the geological cross-section is referenced from the literature (Chen et al., 2018; Cheng et al., 2019a; Cheng et al., 2019b).

In addition, the subsurface media (water, air, soil, rock, etc.) on the hillslopes of the study area exhibit significant differences in physical properties, which are reflected in parameters such as resistivity, relative permittivity, density, and electromagnetic wave velocity (Table 1). This provides a sound geophysical basis and justification for the implementation of ERT experiments.

1.2 Electrical Resistivity Tomography (ERT) method

Electrical Resistivity Tomography (ERT) is a widely applicable geophysical exploration method, commonly used to address issues related to groundwater hydrology, geotechnical structures, and engineering geology. Based on the resistivity

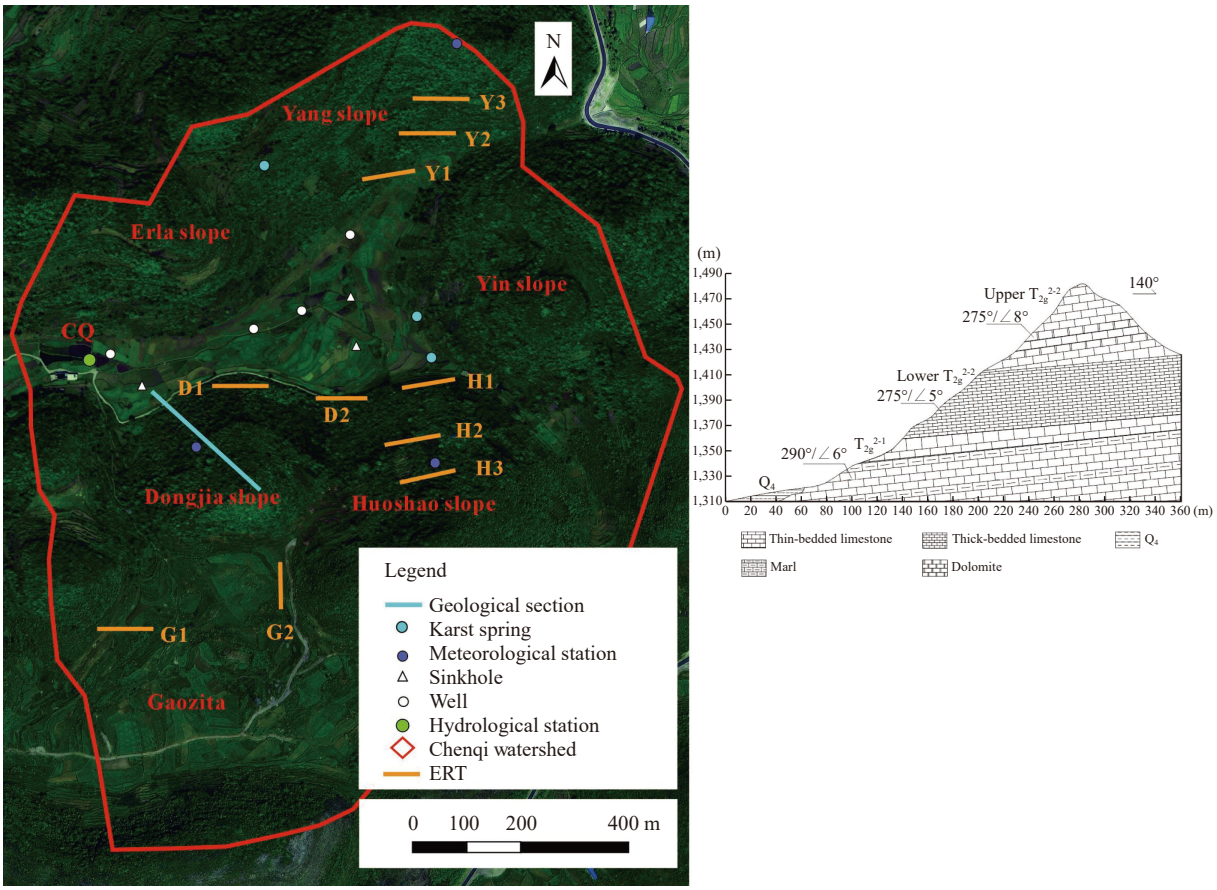


Fig. 1 Geographical and geological description of the Chenqi watershed, including the location of key features: Springs, sinkholes, wells and ERT survey lines

Table 1 Physical properties of the major subsurface media in the study area

Medium	Resistivity/Ω·m	Relative permittivity	Density/g·cm^{-3}	EM wave velocity/m·ns^{-1}
Air	-	1	-	0.30
Water	50–60	80	1.0	0.03
Clay	10–600	5–40	1.6–2.0	0.06
Dolomite	50–6,000	6	2.8–3.0	0.12
Thin-bedded limestone	60–2,000	4–8	2.6–2.8	0.12
Thick-bedded limestone	500–6,000	4–8	2.6–3.1	0.12
Marl	5–5,000	-	2.3–2.5	-

differences of subsurface media (e.g., rocks and soils), it detects the distribution of subsurface media by mapping the resistance distribution in response to an applied direct-current field.

In this ERT survey, a SYSCAL Pro high-density resistivity meter was adopted, equipped with 10 dipole receiver channels, and data acquisition was fully automated. The Wenner array was used for measurement, with a maximum number of acquisition layers of 24. A total of 72 electrodes were deployed during the experiment, with a fixed electrode spacing of 1 m, yielding an effective investigation depth of approximately 12 m. Ten survey lines were arranged across four zones in the Chenqi Small Watershed (detailed information on the survey lines is listed in Table 2, and their field distribution is shown in Fig. 1). Three survey lines were installed on both Yang slope (anti-dip slope) and Huoshao slope (dip slope), covering the upper, middle, and lower positions of the slopes to characterize the overall slope features. Two survey lines were arranged in Gaozita (high-lying depression), located in the central part of the depression to detect the aquifuge. As the survey lines were situated on a hillside, the experiment was conducted on flat abandoned farmland to minimize topographic effects. The survey lines were laid out to the maximum feasible length under field

Table 2 ERT survey lines details in the study area

Location	Slope position	Line No.	Length of survey line/m
Yang slope (anti-dip slope)	Lower slope	Y1	96
	Middle slope	Y2	72
	Upper slope	Y3	72
Huoshao slope (dip slope)	Lower slope	H1	108
	Middle slope	H2	108
	Upper slope	H3	84
Gaozita	High-lying depression	G1	120
	High-lying depression	G2	96
	Slope bottom	D1	72
Verification	Slope bottom	D2	144

conditions, resulting in relatively short and inconsistent lengths. The survey lines on Yang slope and Huoshao slope were laid horizontally along the mountain strike direction. For Gaozita, since the distribution range and depth of the aquiclude were unknown, two mutually perpendicular boundary survey lines were arranged to fully explore its existence and distribution. This ERT survey can meet the requirements for investigating the development and distribution characteristics of surface karst on karst slopes.

In addition, due to the complexity of karst areas, the measuring device was carefully selected for this experiment. The Wenner array is sensitive to vertical layered structures, with strong measurement signals, good data stability, and simple deployment, making it suitable for the overall detection of underground structures. Therefore, it is more practical in most shallow resistivity surveys (Jiang et al., 2025). In contrast, although the dipole-dipole array has higher horizontal resolution, its signals are susceptible to noise interference and the stability of data inversion is poor. The Wenner-Schlumberger array offers a certain balance between vertical and horizontal detection capability, but its electrode arrangement is complex, detection efficiency is low, and its signal characteristics in layered media are not as clear as those of the Wenner array. Considering the detection objectives, site conditions, and data reliability comprehensively, the Wenner array was ultimately adopted.

1.3 Geological drilling

ERT interprets and infers subsurface geological structures based on the apparent resistivity distribution of geotechnical media. Its result accuracy relies on inference methods and interpretation techniques, which entail uncertainties and non-uniqueness, thus requiring verification by other methods. Geological drilling obtains subsurface rock cores via drilling machinery, which can directly reflect the characteristics of subsurface geological structures with authentic and reliable results. However, it has drawbacks such as high costs and restricted deployment conditions. As a common verification method for other exploration techniques, it exhibits remarkable effectiveness in testing the validity and applicability of complementary exploration approaches.

To verify the ERT inversion results, a survey line D1 was deployed at the slope bottom of the Chenqi Small Watershed (Fig. 1), with a relatively short length of 72 m. After completing the inversion and interpretation of ERT data, a borehole location was selected at the 15 m mark of survey line D1, corresponding to a zone of complex vertical resistivity variations revealed by the inversion results. The geological stratigraphic structure established by integrating the documented results of the extracted rock cores, inversion interpretation data, and drilling data is presented in Fig. 2.

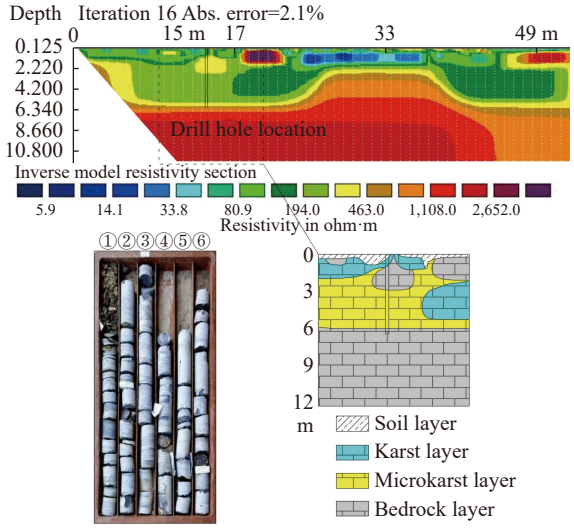


Fig. 2 Validation diagram of stratigraphic structure by geological drilling and ERT inversion

These findings provide direct evidence for the scientific validation of the ERT results.

1.4 Typical outcrops

Due to the scarcity of boreholes in the study area, the interpretation accuracy of ERT is restricted by single borehole verification. Therefore, supplementary verification methods are required. A typical outcrop refers to a well-exposed occurrence of strata, rock masses or structures on the surface that can represent the basic characteristics of regional geological bodies. Owing to road construction at the foot of Dongjia slope, a large area of geological bodies is exposed. Accordingly, line D2 with a total length of 144 m was laid out above the profile. Three typical outcrops were selected along the profile for comparative analysis with ERT results to further verify the feasibility of the method. The ERT inversion results and photographs of the typical outcrops are shown in Fig. 3.

2 Results and analysis

The raw data were acquired and preprocessed using Prosys II software in this experiment. Res2dinv software was employed for ERT inversion, with a grid parameter of 30 layers set to ensure that the inversion images were refined so that each color change within a grid cell corresponds to an approximate depth variation of 0.25 m. The inversion calculation was conducted using the least-squares method, which automatically generated a 2D subsurface resistivity model. Due to the significant difference in resistivity among the soil layer, karstified layer, and intact bedrock, logarithmic values of apparent resistivity were adopted to better reflect the boundaries between them. Finally, after post-processing steps including annotation of the ERT inversion images and delineation of the surface extent (white lines in the figures), the ERT inversion results of all survey lines were obtained (Figs. 4–11).

2.1 Verification of ERT inversion results

The total length of the drill core is 6 m, which is recorded in six sections (1 m per section) with an overall recovery rate exceeding 90% (Fig. 2). The results show that: The soil layer is approximately 0.3 m thick, consistent with the ERT interpretation results; the interval 0.3–1.0 m consists of moderately fractured rock mass with dissolution traces, indicating well-developed karstification; 1.0–1.2 m is characterized by intact rock columns; 1.2–2.1 m is slightly fractured rock mass without dissolution; 2.1–3 m is intact rock mass; 3–5.8 m is relatively intact rock mass with abundant dissolution traces, where karstification is well-developed; 5.8–6.0 m is relatively intact rock mass. The drilling results are highly consistent with the karst development characteristics interpreted by ERT, with minimal errors. Moderately fractured and relatively intact rock masses in non-karst areas were not effec-

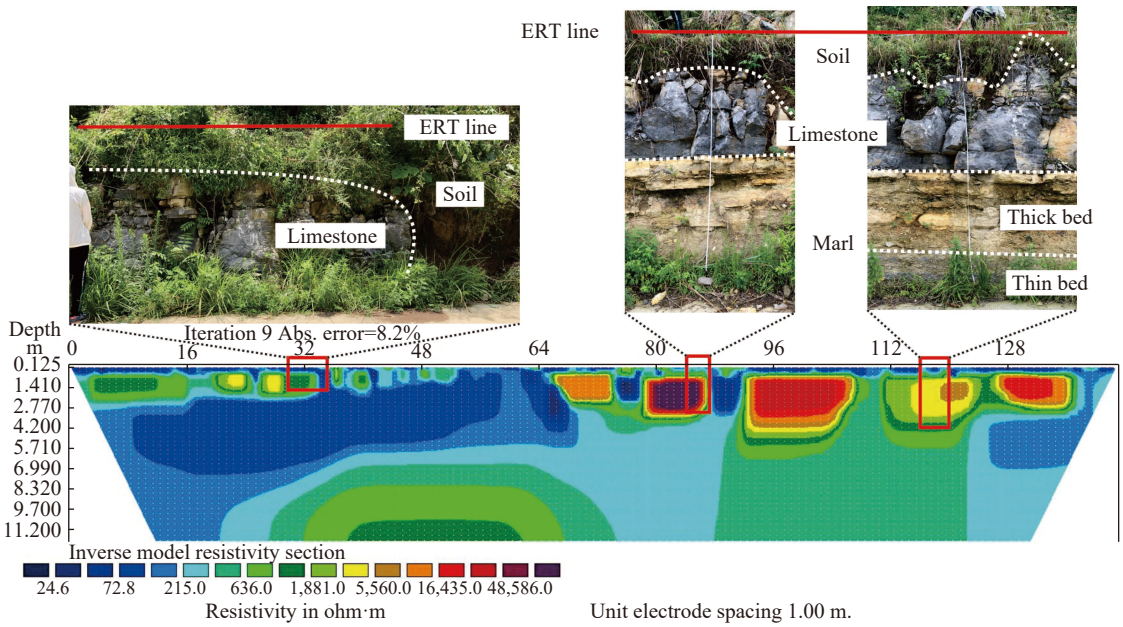


Fig. 3 Typical outcrop verification of ERT inversion results

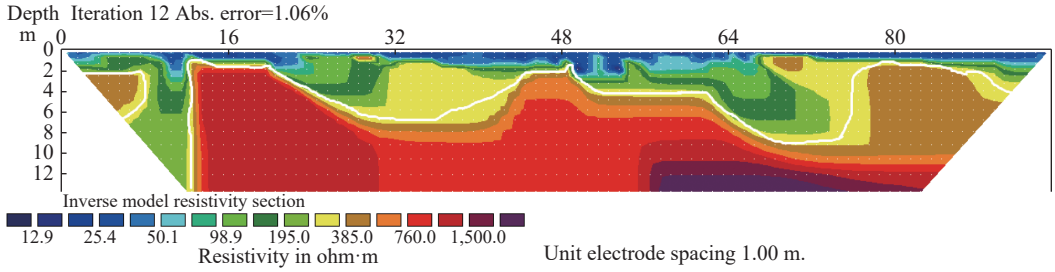


Fig. 4 ERT inversion profile for survey line Y1

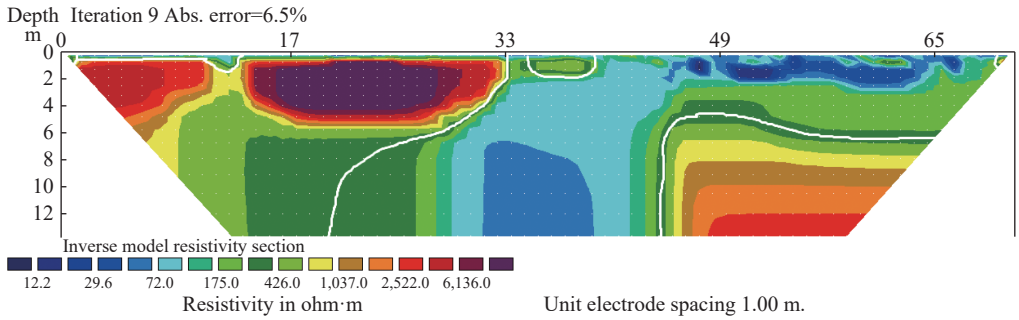


Fig. 5 ERT inversion profile for survey line Y2

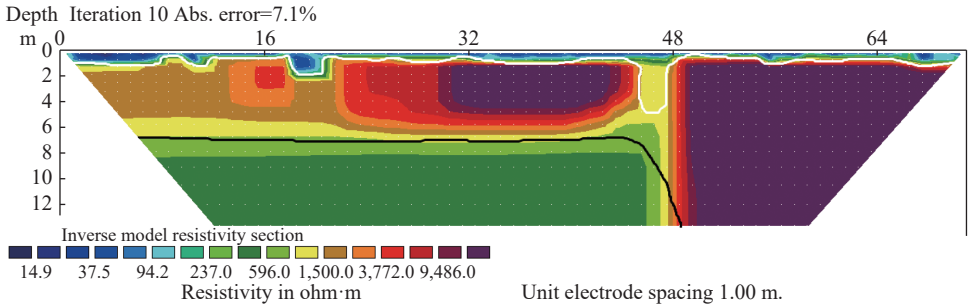


Fig. 6 ERT inversion profile for survey line Y3

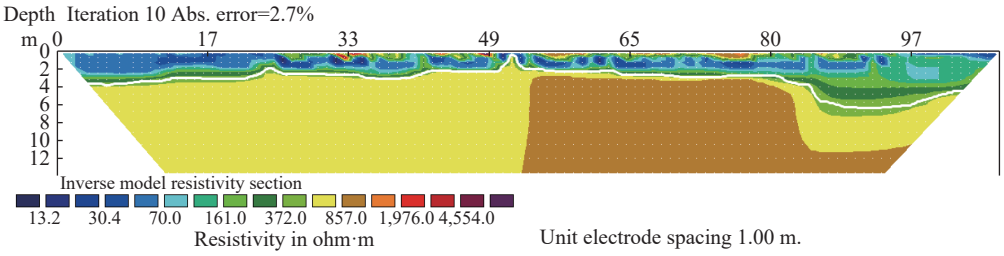


Fig. 7 Inversion map of ERT for survey line H1

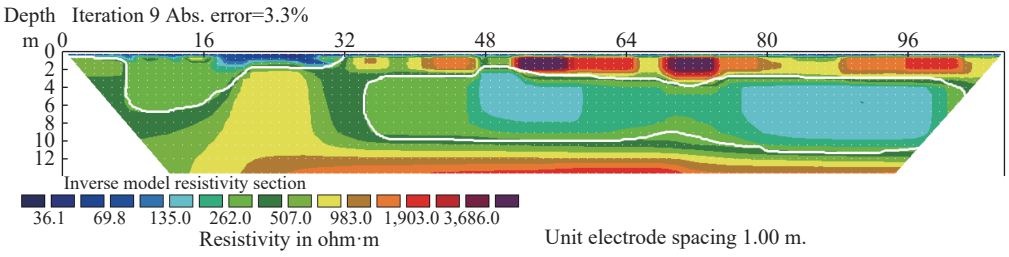


Fig. 8 Inversion map of ERT for survey line H2

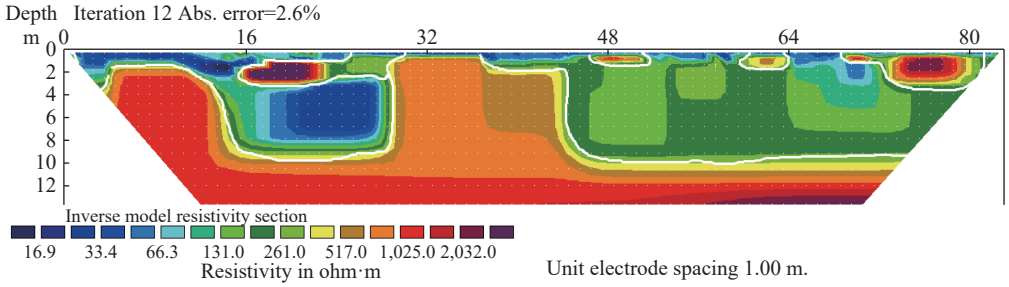


Fig. 9 Inversion map of ERT for survey line H3

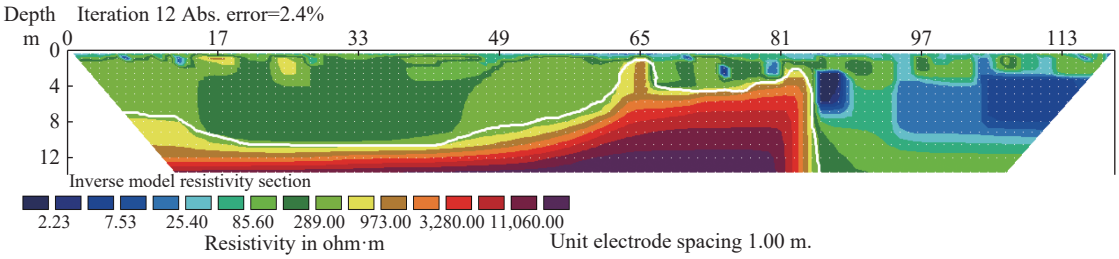


Fig. 10 ERT inversion profile for survey line G1

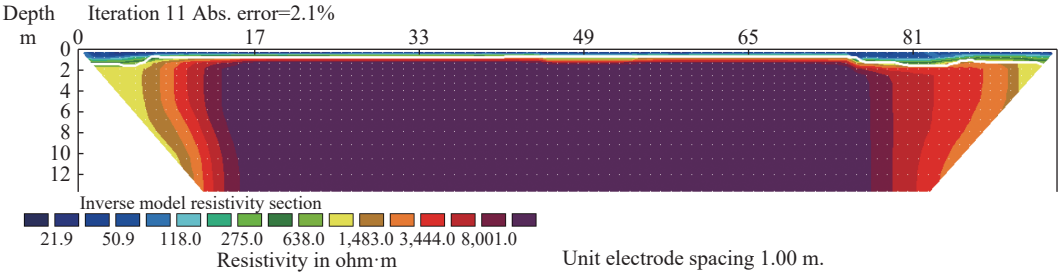


Fig. 11 ERT inversion profile for survey line G2

tively distinguished, presumably due to the small difference in fracturing intensity between them, resulting in no significant difference in resistivity response and making accurate characterization through electrical inversion difficult. The resistivity of karst-developed rock mass is significantly lower than that of the surrounding rock, and rock mass integrity did not affect the identification of karst-developed zones by ERT. In conclusion, ERT inversion exhibits excellent interpretation performance on the limestone slope of the study area, especially in accurately identifying karst development locations, which can meet the research requirements.

Fig. 3 illustrates the correspondence between the ERT inversion profile and geological outcrops, aiming to verify the reliability of geophysical exploration using field geological observations. Typical outcrops were selected at 32 m, 85 m, and 118 m along Profile D2. The ERT survey line is marked by a solid red line, while the soil–rock interface and lithological boundaries are indicated by dashed white lines. The visible geological units at each outcrop are, in sequence: Soil, limestone, thick marl, thin marl, and limestone. The results show that the resistivity characteristics of soil, limestone, marl, and other media are highly consistent with the ERT inversion results, with only minor deviations in the distribution of soil. These deviations mainly result from a horizontal offset of approximately 0.25 m between the survey line layout and the outcrop, as well as weathering, erosion, and soil infiltration affecting the outcrops, leading to slight differences between the ERT detection results and field geological observations. A sharp decrease in resistivity at 34 m corresponds to the boundary between bedrock and soil-infiltrated zones in the outcrop profile. A high-resistivity anomaly at 85 m coincides with the marl aquiclude, providing a basis for interpreting the widespread high-resistivity characteristics of the high-lying depression. Below the 118 m mark, the resistivity shows a trend of first increasing and then decreasing, corresponding to the transition from thick marl

to thin marl. This indicates that thick marl has a higher resistivity than thin marl, and thick marl is more likely the main body of the aquiclude. These findings clarify the resistivity ranges of soil, limestone, and marl, and can provide a reference for the interpretation of ERT survey results.

2.2 ERT inversion results of the anti-dip slope

Fig. 4 presents the ERT inversion results of the lower-slope survey line Y1 on the anti-dip slope. The transition zone from low resistivity to high resistivity in the figure is inferred to be the epikarst zone, while the blue and light blue areas generally represent soil zones. The results indicate that rock strata with resistivity values less than approximately 300 Ω·m are karst-developed. Karstification occurs at nearly the surface at multiple locations (e.g., 16 m, 48 m, 80 m), and the depth of karst development varies across other regions, demonstrating high heterogeneity and discontinuity of karstification.

Survey line Y2 on the midslope of the anti-dip slope (Fig. 5) shows a distinctive low-resistivity anomaly. Compared with other survey lines, it is characterized by the coexistence of conduit-type low resistivity and near-surface low resistivity. Specifically, part of the karst develops beneath intact rock strata with a pipe-like shape, rather than the typical distribution between the soil layer and intact bedrock. It is inferred that such conduit-type karst serves as both a migration channel for karst water and undergoes further karstification under water seepage and erosion. The high-resistivity anomaly in the surface layer of the latter half of the survey line is attributed to the dense distribution of surface rocks. Interpretation results show that the soil layer in the first half of the survey line is extremely thin with underdeveloped karst, while the soil thickness in the latter half increases significantly with a simultaneous increase in karst development depth. This indicates significant spatial variability in soil thickness across the karst limestone area, with a certain positive correlation between epikarst thickness and soil thickness.

Based on the stratigraphic lithology of the study area, the upper part of the sunny slope is the boundary between thin-bedded limestone and thick-bedded limestone, where the anti-dip slope survey line Y3 (Fig. 6) is exactly located. The ERT inversion results of Y3 show that the epikarst zone in the upper slope is shallow, concentrated approximately 0.5 m below the soil layer. Notably, the ERT inversion clearly depicts the boundary between thin-bedded limestone and thick-bedded limestone (black line in Fig. 6). At the horizontal interval of 0–48 m and a depth of 7 m in this survey line, the resistivity of the overlying strata is significantly higher than that of the underlying strata. Since the overall resistivity in this region is relatively high (approximately > 400 Ω·m), this phenomenon is not caused by karst development. Instead, it is inferred to result from the resistivity difference between the two limestone facies, i.e., the thin-bedded limestone beneath the intact rock layer has a lower resistivity than the thick-bedded limestone.

In summary, the ERT inversion achieves excellent performance on the anti-dip slope, and it is feasible to infer the actual karst development based on the inversion results. Karstification exhibits high heterogeneity with discontinuous development of the epikarst zone; pipe-shaped karst is prone to occur in the middle slope, which also serves as a migration channel for karst water. ERT inversion also demonstrates outstanding effectiveness in identifying two limestone lithological types with high accuracy in determining the stratum boundary.

2.3 ERT inversion results of the dip slope

Figs. 7, 8, and 9 present the ERT inversion results of the lower-slope, middle-slope, and upper-slope positions of the Huoshao slope, respectively. Influenced by variations in subsurface rock fracturing, karst development intensity, and lithological purity across different elevations, the maximum resistivity values of each survey line vary significantly. With increasing elevation, the average rock resistivity shows a decreasing trend, indicating a higher degree of rock weathering in the upper slope. This variation pattern is exactly opposite to that of the anti-dip slope, reflecting that factors such as mountain topography and slope aspect can regulate the direction of water movement, thereby affecting karst development. The H1 survey line (Fig. 7) is dominated by epikarst, characterized by shallow and uniform development depth. Dense surface rocks result in multiple surface high-resistivity anomalies, which to a certain extent reduce water infiltration and weaken the erosion of subsurface rocks and the intensity of karst development.

Similar to the Y2 survey line on the anti-dip slope (Fig. 5), the middle-slope H2 survey line on

the dip slope (Fig. 8) also develops pipe-shaped karst with a more extensive distribution. Local epikarst occurs before the 32 m mark of the survey line, while the latter segment is entirely composed of pipe-shaped karst. Compared with the anti-dip slope, the karst areas of the H2 survey line exhibit lower average resistivity, more intact pipe morphology (not connected to the surface), and a tendency to expand laterally. The resistivity on both sides of the pipe is lower than that in the center, with traces of incomplete development. It is inferred that two karst conduits merged into one during the lateral erosion process. This result further confirms that driven by water movement, pipe-shaped karst continuously erodes laterally and downward from the pipe core outward, eventually forming larger karst conduits.

The H3 survey line (Fig. 9) is laid on the upper slope of the Huoshao slope, and its ERT inversion results are highly typical, covering all types of karst development in the study area. The 0–16 m segment of the survey line develops shallow karst with a relatively thick soil layer; the 16–32 m segment is a pipe-shaped karst development area, where the pipe center has extremely low resistivity, possibly indicating a sediment-filled karst cave; the 32–40 m segment shows almost no karst development, reflecting the discontinuous distribution of the epikarst zone; the latter segment of the survey line has a large karst development thickness and dense surface rocks. Affected by discontinuous rocks, water preferentially infiltrates through the gaps between gravels, causing differential dissolution and gradually forming the rudiments of solution pipes. This phenomenon also explains the core reason for the significant resistivity differences within the same karst area.

In summary, the ERT inversion achieves excellent performance on the dip slope, with many similarities to the anti-dip slope. Pipe-shaped karst develops in the middle-slope position of both slopes, providing favorable conditions for karst water migration; the development intensity of epikarst is irrelevant to elevation, but surface rocks, soil thickness, subsurface rock fragmentation, and geological structures can affect karst development to a certain extent; the scope and intensity of karst development will gradually increase under the erosion of preferential flow.

2.4 ERT inversion results of the high-lying depression

Both the G1 survey line (Fig. 10) and G2 survey line (Fig. 11) exhibit extremely high maximum resistivity values, confirming the extensive distribution of an impermeable layer. The ERT inversion successfully delineated the location of the regional impermeable layer, providing new insights into the geomorphological evolution of the study area.

The G1 survey line is situated west of Gaozita, near the watershed boundary. Further west, the terrain descends with concentrated surface gullies (the theoretical termination zone of the impermeable layer). The ERT inversion results show that G1 exhibits a relatively deep low-resistivity anomaly, indicating the extensive development of underground karst. A uniform high-resistivity zone appears at a depth of 12 m (4 m depth in the 60–80 m segment of the survey line), which is identified as the regional impermeable layer. The resistivity difference between the upper and lower layers reaches nearly 10,000 Ω·m, a phenomenon not observed in the slope survey lines. This further underscores the critical role of the impermeable layer in the formation of depression landforms during karst evolution. The 84 m mark of the survey line corresponds to the termination of the impermeable layer and serves as a groundwater discharge pathway. Sustained downward karstification at this location has resulted in deep karst development.

The G2 survey line is located northeast of Gaozita, adjacent to the Huoshao slope, where the rock exposure rate is relatively high. Theoretically, the impermeable layer should be extensively distributed here. ERT inversion results show that the impermeable layer is widely distributed across the entire survey line, occurring at a depth of approximately 1 m. The front section of the survey line is near the crest of the Huoshao slope, where a low-resistivity zone is observed at 10 m depth, corresponding to a karst-developed area and representing the starting point of the impermeable layer. A low-resistivity anomaly also appears in the rear section of the survey line, but it is not interpreted as karst-related. This is presumably due to rock fracturing near the edge of the impermeable layer or significant errors in the ERT inversion.

In summary, the ERT exhibits excellent performance in delineating subsurface impermeable layers in karst areas, enabling accurate detection of aquiclude depth and spatial extent. For depressions within karst watersheds, the presence of impermeable layers blocks downward water erosion and regulates the direction of karst water movement, which plays a crucial role in the study of groundwater dynamics in karst regions.

2.5 ERT 3D inversion results

ERT profile inversion suffers from the non-uniqueness problem in geological interpretation, and 3D resistivity inversion serves as one of the important verification methods. Given the large spacing of survey lines in the study area and their distribution on slope surfaces with different elevations, full-watershed 3D observation is difficult to implement. In this study, the main survey line Y1 was selected to conduct small-scale 3D resistivity joint inversion, aiming to improve the spatial representativeness and interpretation reliability of the results. The 3D observation adopted the Wenner array, which was deployed on both sides of the Y1 survey line to form a 3D observation grid. The inversion was carried out using the RES3DINV software, and the final RMS error was 2.72% after 6 iterations, meeting the convergence criteria. The 3D inversion results (Fig. 12) are presented in the form of depth slices (15 layers in total), allowing direct comparison with the 2D inversion results (Fig. 4).

The results show that the shallow layer (0–2.50 m) is dominated by low resistivity, corresponding to loose soil. The 3D slices reveal spatial heterogeneity in soil thickness (no soil cover at the 30 m position in some areas), which is consistent with the variation in soil thickness revealed by profile inversion. The middle layer (2.50–8.39 m) exhibits a complex mosaic distribution of resistivity. The 3D slices clearly show the planar distribution of karst-developed zones and water-bearing fracture zones. A local low-resistivity anomaly is observed at a horizontal distance of 50–70 m in both 2D inversion and 3D slices, which verifies the accuracy of the profile interpretation. The deep layer (8.39–23.8 m) is characterized by overall high resistivity with little fluctuation. Both 3D and 2D results reflect the stable structural features of intact deep bedrock with low water content. 3D inversion overcomes the limitation of the strip-like perception from 2D profiles and directly presents the planar extent and connectivity of karst zones. Meanwhile, the planar distribution of local low-resistivity anomalies in the 3D results further corroborates the spatial location of groundwater enrichment areas and improves the integrity of geological interpretation. However, constrained by topographic relief of mountain slopes and the layout range of electrode arrays, 3D inversion is inferior to 2D profile inversion in identifying karst distribution at the watershed scale. Therefore, 2D profile inversion remains the core method in this study.

The 3D inversion results do not replace the 2D profile inversion, but provide supplementary verification through an additional spatial dimensions. On the one hand, the vertical zonation characteristics are highly consistent with those of profile inversion, confirming the reliability of the layered structure consisting of surface soil, middle karst zone, and deep bedrock. On the other hand, the spatial distribution of anomalous areas revealed by horizontal slices provides direct three-dimensional constraints for the geological model shown in Fig. 13, and clarifies the horizontal extension and verti-

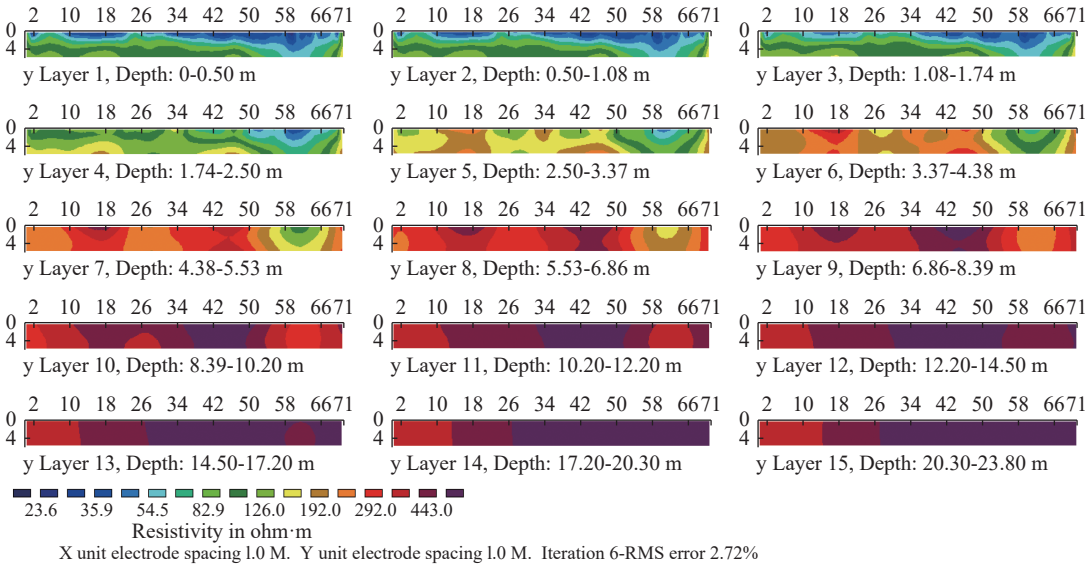


Fig. 12 3D ERT inversion results for survey line Y1 (horizontal axis: Survey line length; vertical axis: Horizontal distance; layers 1–15: Slices at different depths)

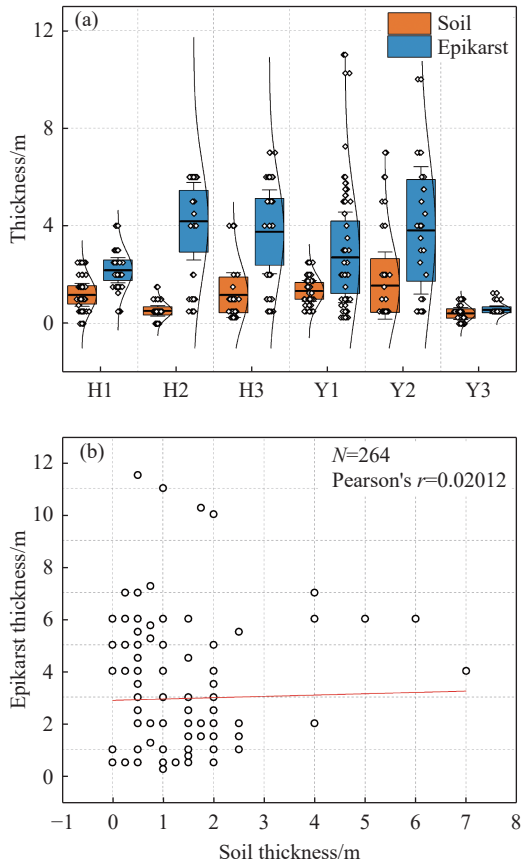


Fig. 13 Statistics of slope soil and epikarst thickness (a), and the relationship between soil thickness and epikarst thickness analyzed based on sampling points (b, where N is the number of samples and r is the correlation coefficient)

cal connectivity of the karst-developed zones. The combination of the two methods allows a more accurate assessment of geological structures and groundwater distribution, providing a more reliable scientific basis for groundwater exploration and karst detection. However, in karst areas with complex geology and topography, high-density profile inversion may be more adaptable than small-scale 3D inversion.

2.6 Soil and karst distribution characteristics

Based on six ERT inversion profiles across the slope (H1, H2, H3, Y1, Y2, Y3), statistical analyses were performed on soil thickness and epikarst thickness using 264 sampling points (Fig. 13). The results show that the slope soil thickness in the study area is generally thin, with a median value of approximately 0.5–2.0 m and a maximum observed thickness not exceeding 3.0 m. In stark contrast, the epikarst thickness is significantly larger, with a median range of 2.0–4.0 m and extreme values reaching up to −12 m at profiles such as Y1 and Y2. Spatially, the epikarst thickness at the midslope position is notably higher than that at other slope positions, while the soil thickness shows no significant difference among different slope positions. This distribution pattern clearly indicates that the epikarst zone is the dominant host layer of subsurface space in karst watersheds, and its spatial distribution is characterized by strong heterogeneity. Furthermore, a weak positive correlation exists between soil thickness and epikarst thickness (Fig. 13b), suggesting that these two layers may have undergone co-development during karst geomorphological evolution, collectively forming a complex karst subsurface structural system.

3 Discussion

3.1 Comparison of ERT inversion results for different slopes

Fig. 14 illustrates the subsurface structures of the anti-dip slope and dip slope in the Chenqi Small Watershed as revealed by ERT inversion results. Vertically along each survey line, the stratigraphic sequence from the surface to the subsurface consists of the soil layer, karst layer, and limestone bedrock layer, which is a typical structural characteristic of the epikarst zone. Both slopes share a similar stratigraphic structure, but the distribution and morphology of the karst layer differ. For the anti-dip slope (left of Fig. 14), obvious karst development occurs between 40 m and 50 m along each survey line; for the dip slope (right of Fig. 14), significant karst development is also observed after 40 m along each survey line, and these areas serve as karst water flow paths. The distribution of surface rocks and soil thickness also exhibits both similarities and differences, which are all factors influencing karst development.

The downhill extension of the karst layer on the anti-dip slope may pose a threat to geological stability, particularly in areas with karst caves. In contrast, the karst layer on the dip slope is relatively scattered, which may have a lesser impact on geological stability, but the presence of karst caves still requires attention. The karst layers on both slopes may exert a continuous influence on groundwater flow and soil conditions, necessitating further environmental assessments. By comparing the ERT inversion results of these two

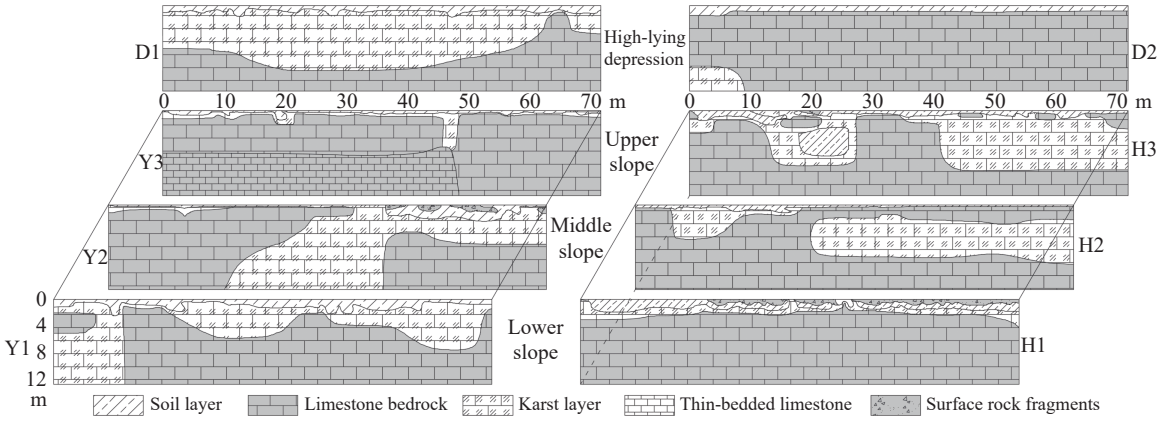


Fig. 14 Structural interpretation of the watershed based on ERT inversion results

slopes, a better understanding of subsurface structures and potential geological issues under different geological conditions can be achieved. This holds significant implications for land use planning, groundwater hydrological processes, and environmental protection.

3.2 Application of ERT inversion in Karst watersheds

In this study, different geological bodies are interpreted based on resistivity contrasts. Typically, limestone bedrock exhibits high resistivity, while karst layers and thin-bedded limestone have low resistivity (Ryckebusch et al., 2025). The resistivity variations of the two slopes are similar, but differences in lithology and rock structure may lead to slight discrepancies in resistivity values. Such resistivity contrasts enable ERT to perform effectively in detecting karst distribution characteristics in karst areas. For different geological backgrounds and research requirements, various experimental approaches can be adopted to achieve specific objectives. For instance, ERT cross-sections can reveal resistivity changes, where low-resistivity zones correspond to water-bearing layers, and comprehensive parameters derived from electrical inversion can effectively characterize the coupling relationship between aquifer thickness and water quality (Obiora and Ibuot, 2023; Song et al., 2025). Additionally, integrated geophysical methods including ERT can be used to detect groundwater infiltration and discharge paths, as these are the primary factors contributing to the formation of sliding zones within low-resistivity water-bearing structures prone to landslides (Yu et al., 2023).

Although this study represents a basic application of the ERT method, to fully investigate the karst development characteristics of the entire watershed, various terrains, slope types, and geomorphic units in a typical karst watershed were selected, including dip slopes, anti-dip slopes, and high-lying depressions. Furthermore, different elevation positions of individual slopes were fully considered, ensuring that the results comprehensively reflect the karst development characteristics at the entire karst watershed scale. ERT inversion technology holds significant application value in karst watersheds for detecting groundwater flow, soil-superficial karst interfaces, and geological structures. By innovating experimental design, selecting appropriate methods, or integrating with other techniques, a more comprehensive assessment and utilization of water resources in karst areas can be achieved.

3.3 Impact of karst development on groundwater resources

Geological structures, climate, topography, and hydrological characteristics exert significant influences on groundwater resources (Cheng et al., 2024). In karst areas, karst development plays a crucial role in regulating groundwater flow (Guo et al., 2025). Within karst water systems, groundwater tends to flow along fractures and erosion-prone pathways. Over time, the flow gradually transitions to a turbulent state and concentrates into a limited number of major channels, forming karst conduits. ERT surveys in this study detected karst conduits in the middle sections of both slopes, which serve as indicators of karst water migration pathways. This is consistent with the findings of most current scholars (Hao et al., 2025; Huang et al., 2025). However, due to the high velocity and turbulent nature of groundwater flow in karst conduits, these structures accumulate most of the water resources in the aquifer. Such karst conduits also pose challenges to the stability of mountain

slopes in karst regions, while the concentrated flow pattern holds important implications for water resource management and protection (Bo and Mei, 2018; Li et al., 2023). Therefore, research on pipe-shaped karst and fractures within karst layers is essential for understanding and predicting karst water flow, as well as formulating corresponding water resource management strategies.

Karst regions are characterized by thin soil layers and highly permeable karst aquifers, resulting in poor stability of the water-bearing system, which is vulnerable to external disturbances (Zhang et al., 2020). These factors render karst groundwater susceptible to pollution, thereby affecting water quality (Lan et al., 2024). Contamination of karst water can disrupt the balance of aquatic ecosystems, leading to unforeseen ecological changes (Atoui and Agoubi, 2026). Consequently, changes in the geological environment of karst areas have significant impacts on the ecological system. Specifically, variations in groundwater resources affect regional hydrological cycles, exacerbate surface water scarcity, and threaten biodiversity. Alterations to the geological environment may also trigger geological hazards such as ground subsidence, landslides, and rockfalls, posing severe risks to the ecological environment and human life and property safety.

The impacts of karst development on groundwater resources in karst watersheds are multifaceted, and these influencing factors must be fully considered in groundwater resource management and environmental protection.

4 Conclusions

(1) ERT exhibits excellent performance in detecting karst distribution characteristics and accurately delineating the location of impermeable layers in karst watersheds. Three-dimensional (3D) inversion provides a more comprehensive representation of subsurface structures within small-scale areas, while 2D cross-sectional inversion focuses more on specific geological information and is better suited for karst detection at the watershed scale. Geological drilling technology effectively verifies the validity and applicability of ERT.

(2) Karst development in karst watersheds is highly heterogeneous, with discontinuous development of epikarst zones. Pipe-shaped karst is prone to occur in the middle slope positions of karst watershed slopes, serving as indicators of karst water migration directions. The intensity and scope of karst development will gradually expand under water erosion, further influencing groundwater resources in karst areas. Karst water is dominated by runoff on dip slopes whereas infiltration dominates on anti-dip slopes; continuous low-resistivity aquicludes in high-lying depressions control local groundwater levels. Karst structure and groundwater runoff show a coupled synergistic relationship under the control of topographic differentiation.

(3) The average soil thickness is approximately 0.5–2.0 m, and the average thickness of the epikarst zone is about 2.0–4.0 m. There is a weak positive correlation between soil thickness and epikarst zone thickness. The scientific application of ERT combined with geological drilling can effectively detect karst development characteristics in karst watersheds, providing quantitative results for karst research. This approach also holds significant implications for hydrological response processes, groundwater regulation and storage, and ecological environmental protection.

Acknowledgements

This study was supported by Key Research and Development Program of Hunan Provincial Department of Science and Technology (No. 2022SK2073) and Young Scientists Fund of the National Natural Science Foundation of China (No. 42407118).

References

An R, Li B, Li J, et al. 2026. Quantifying the vulnerability of karst groundwater to emerging organic compounds in southwest China. Environmental Pollution, 388: 127374. DOI：10.1016/j.envpol.2025.127374.

Atoui M, Agoubi B. 2026. Vulnerability assessment in fractured aquifer using improved vulnerability index: Applied to Gabes aquifer, Southeastern Tunisia. Journal of Groundwater Science and Engineering, 14(1): 69−82. DOI：10.26599/jgse.2026.9280073.

Bermejo L, Ortega AI, Parés JM, et al. 2020. Karst features interpretation using ground-penetrating radar: A case study from the Sierra de Atapuerca, Spain. Geomorphology, 367: 107311. DOI：10.1016/j.geomorph.2020.107311.

Bo L, Mei LX. 2018. Characteristics of karst groundwater system in the northern basin of

Laiyuan Spring area. Journal of Groundwater Science and Engineering, 6(4): 261−269. DOI: 10.19637/j.Cnki.2305-7068.2018.04.002.

Bouzerda M, Mehdi K, Fadili A, et al. 2026. Electrical resistivity tomography involvement to investigate collapse dolines in Mogress area, Doukkala plain (Western Morocco). Catena, 263: 109742. DOI: 10.1016/j.catena.2025.109742.

Cao JH, Wu X, Huang F, et al. 2018. Global significance of the carbon cycle in the karst dynamic system: Evidence from geological and ecological processes. China Geology, 1(1): 17−27. DOI: 10.31035/cg2018004.

Chen X, Zhang ZC, Soulsby C, et al. 2018. Characterizing the heterogeneity of karst critical zone and its hydrological function: An integrated approach. Hydrological Processes, 32(19): 2932−2946. DOI: 10.1002/hyp.13232.

Cheng QB, Chen X, Tao M, et al. 2019a. Characterization of karst structures using quasi-3D electrical resistivity tomography. Environmental Earth Sciences, 78(9): 285. DOI: 10.1007/s12665-019-8284-2.

Cheng QB, Tao M, Chen X, et al. 2019b. Evaluation of electrical resistivity tomography (ERT) for mapping the soil–rock interface in karstic environments. Environmental Earth Sciences, 78(15): 439. DOI: 10.1007/s12665-019-8440-8.

Cheng QY, Wang SJ, Peng T, et al. 2020. Sediment sources, soil loss rates and sediment yields in a Karst plateau catchment in Southwest China. Agriculture, Ecosystems and Environment, 304: 107114. DOI: 10.1016/j.agee.2020.107114.

Cheng YP, Zhang FW, Dong H, et al. 2024. Groundwater and environmental challenges in Asia. Journal of Groundwater Science and Engineering, 12(2): 223−236. DOI: 10.26599/jgse.2024.9280017.

Coulouma G, Lagacherie P, Samyn K, et al. 2013. Comparisons of dry ERT, diachronic ERT and the spectral analysis of surface waves for estimating bedrock depth in various Mediterranean landscapes. Geoderma, 199: 128−134. DOI: 10.1016/j.geoderma.2012.07.026.

Funk B, Flores-Orozco A, Steiner M. 2024. Possibilities and limitations of cave detection with ERT. Geomorphology, 462: 109332. DOI: 10.1016/j.geomorph.2024.109332.

Gao QS, Wang SJ, Peng T, et al. 2020. Evaluating the structure characteristics of epikarst at a typical peak cluster depression in Guizhou plateau area using ground penetrating radar attributes. Geomorphology, 364: 107015. DOI: 10.1016/j.geomorph.2019.107015.

Guo F, Jiang GH, Yuan DX, et al. 2013. Evolution of major environmental geological problems in karst areas of Southwestern China. Environmental Earth Sciences, 69(7): 2427−2435. DOI: 10.1007/s12665-012-2070-8.

Guo GH, Ji ZY, Chen LH, et al. 2025. Experimental and numerical analyses of nonlinear conduit-matrix exchange flow mechanism in heterogeneous karst aquifers. Journal of Hydrology, 661: 133623. DOI: 10.1016/j.jhydrol.2025.133623.

Guo YL, Huang F, Chi FX, et al. 2024. Hydrogeological structures of karst features using hydrographs in an underground river basin formed in a peak cluster depression, southwest China. Journal of Hydrology, 634: 131085. DOI: 10.1016/j.jhydrol.2024.131085.

Hao HQ, Zhang J, Illman WA, et al. 2025. Insight into karst hydrological processes in the frequency domain: Critical frequency, phase difference, causality, and machine learning model. Journal of Hydrology, 663: 134150. DOI: 10.1016/j.jhydrol.2025.134150.

Huang FY, Gao Y, Zhang ZZ, et al. 2025. Simulating precipitation-induced karst-stream interactions using a coupled Darcy–Brinkman–Stokes model. Hydrology and Earth System Sciences, 29(22): 6285−6307. DOI: 10.5194/hess-29-6285-2025.

Jiang WW, Peng T, Zhang XB, et al. 2025. High-resolution electrical resistivity tomography for quantitative interpretation of sub-surface karst structures: A case study in Southwest China. Geoderma, 461: 117460. DOI: 10.1016/j.geoderma.2025.117460.

Lan FN, Zhao Y, Li J, et al. 2024. Health risk assessment of heavy metal pollution in groundwater of a karst basin, SW China. Journal of Groundwater Science and Engineering, 12(1): 49−61. DOI: 10.26599/jgse.2024.9280005.

Li QS, Kang XB, Xu M, et al. 2023. Effects of coal mining and tunnel excavation on groundwater flow system in karst areas by modeling: A case study in Zhongliang Mountain, Chongqing, Southwest China. Journal of Groundwater Science and Engineering, 11(4): 391−407. DOI：10.26599/jgse.2023.9280031.

Li S, Wu X, Sun FM, et al. 2022. Environmental geological problems in southwest China: A case study from the researches of regional landslide hazards. Nature Environment and Pollution Technology, 21(1): 159−165. DOI：10.46488/nept.2022.v21i01.017.

Liu Y, Liu Z, Zhang C, et al. 2024. Study on spatial structure characteristics of epikarst zone interpreted by integrated geophysical method: Taking the slope runoff field of Guohua town ecological experiment base in Pingguo City, Guangxi as an example. Carsologica Sinica, 43(01): 209−218. DOI：10.11932/karst20240109.

Luo ZD, Lian JJ, Nie YP, et al. 2024. Improving soil thickness estimations and its spatial pattern on hillslopes in karst forests along latitudinal gradients. Geoderma, 441: 116749. DOI：10.1016/j.geoderma.2023.116749.

Obiora DN, Ibuot JC. 2023. Electrical geophysical evaluation of susceptibility to flooding in University of Nigeria, Nsukka main campus and its environs, Southeastern Nigeria. Journal of Groundwater Science and Engineering, 11(4): 422−434. DOI：10.26599/jgse.2023.9280033.

Ryckebusch C, Baltassat JM, Legchenko A, et al. 2025. Characterization of a heterogeneous limestone vadose zone based on a multimethod and multiscale geophysical approach. Near Surface Geophysics, 23(6): 555−571. DOI：10.1002/nsg.70026.

Song HW, Xia F, Wang WQ, et al. 2025. ANN-based prediction model for single-hole water inflow from piedmont to inland plain areas of Hebei Province, North China Plain. Journal of Groundwater Science and Engineering, 13(4): 434−448. DOI：10.26599/jgse.2025.9280064.

Tao M, Chen X, Cheng QB, et al. 2022. Evaluating the joint use of GPR and ERT on mapping shallow subsurface features of karst critical zone in southwest China. Vadose Zone Journal, 21(1): e20172. DOI：10.1002/vzj2.20172.

Tan Y, Qi J., Xu M, et al. 2024. Application of fractal characteristics of drill hole karst geology in analyzing the degree of karst development. Geological Journal of China Universities, 30(05): 603−612. DOI：10.16108/j.issn1006-7493.2023052.

Wanaim A, Ikirri M, Boutaleb S, et al. 2025. Non-Invasive imaging of subsurface karst architecture using electrical resistivity tomography: A case study from carbonate terranes in Semi-Arid regions (Fouzart cave, Western Anti-Atlas, Morocco). Carbonates and Evaporites, 40(3): 111. DOI：10.1007/s13146-025-01147-4.

Wang F, Nie Y, Chen H, et al. 2024b. Spatial heterogeneity characteristics of soil-epikarst thickness in a typical karst dolomite small watershed. Bulletin of Geological Science and Technology, 43(01): 306−314. DOI：10.19509/j.cnki.dzkq.tb20220399.

Wang M. 2024a. Accelerating collaborative innovation in hydrological, engineering, and environmental fields. Journal of Groundwater Science and Engineering, 12(1): 1−3. DOI：10.26599/jgse.2024.9280001.

Xiao X, Zhang S, Guo W, et al. 2023. Environmental pollution characteristics of surface water and groundwater in southwest China and its research prospects. Earth and Environment, 51(05): 564−573. DOI：10.14050/j.cnki.1672-9250.2023.51.005.

Xie J, Liu Y, Lu YL, et al. 2022. Application of the high-density resistivity method in detecting a mined-out area of a quarry in Xiangtan City, Hunan Province. Frontiers in Environmental Science, 10: 1068956. DOI：10.3389/fenvs.2022.1068956.

Yu FD, Qiao G, Wang K, et al. 2023. Investigation of groundwater characteristics and its influence on Landslides in Heifangtai Plateau using comprehensive geophysical methods. Journal of Groundwater Science and Engineering, 11(2): 171−182. DOI：10.26599/jgse.2023.9280015.

Yue YM, Yuan S, Wang L, et al. 2026. Maize cultivation and forest collapse over five centuries in Southern China. Communica-

tions Earth and Environment, 7: 190. DOI：10.1038/s43247-026-03224-5.

Zhang C, Hou XW, Li XQ, et al. 2020. Numerical simulation and environmental impact prediction of karst groundwater in Sangu Spring Basin, China. Journal of Groundwater Science and Engineering, 8(3): 210−222. DOI：10.19637/j.Cnki.2305-7068.2020.03.002.

Zhang J, Sirieix C, Genty D, et al. 2024. Imaging hydrological dynamics in karst unsaturated zones by time-lapse electrical resistivity tomography. Science of the Total Environment, 907: 168037. DOI：10.1016/j.scitotenv.2023.168037.

Zhang ZC, Chen X, Chen XH, et al. 2013. Quantifying time lag of epikarst-spring hydrograph response to rainfall using correlation and spectral analyses. Hydrogeology Journal, 21(7): 1619−1631. DOI：10.1007/s10040-013-1041-9.

Zhang ZC, Chen X, Cheng QB, et al. 2019. Storage dynamics, hydrological connectivity and flux ages in a karst catchment: Conceptual modelling using stable isotopes. Hydrology and Earth System Sciences, 23(1): 51−71. DOI：10.5194/hess-23-51-2019.

Zhao LS, Hou R. 2019. Human causes of soil loss in rural karst environments: A case study of Guizhou, China. Scientific Reports, 9: 3225. DOI：10.1038/s41598-018-35808-3.